In Situ Study of Atomic Structure Transformations of Pt–Ni Nanoparticle Catalysts during Electrochemical Potential Cycling

Xenia Tuaev,[†,‡,*] Stefan Rudi,[†] Valeri Petkov,[§] Armin Hoell,[⊥] and Peter Strasser[†,*]

[†]Technical University Berlin, Strasse des 17. Juni 124, 10623 Berlin, Germany, [‡]PhotoCatalytic Synthesis Group, Faculty of Science and Technology, University of Twente, P.O. Box 217, 7500 AE Enschede, The Netherlands, [§]Dow 203, Department of Physics, Central Michigan University, Mt. Pleasant, Michigan, United States, and [⊥]Helmholtz-Zentrum Berlin, Albert-Einstein-Strasse 15, 12489 Berlin, Germany. The experiments were designed and carried out by X.T, P.S., S.R., V.P., and A.H. The manuscript was written by all authors. All authors have given approval to the final version of the manuscript.

ABSTRACT When exposed to corrosive anodic electrochemical environments, Pt alloy nanoparticles (NPs) undergo selective dissolution of the less noble component, resulting in catalytically active bimetallic Pt-rich core–shell structures. Structural evolution of $PtNi_6$ and $PtNi_3$ NP catalysts during their electrochemical activation and catalysis was studied by *in situ* anomalous small-angle X-ray scattering to obtain insight in element-specific particle size evolution and time-resolved insight in the intraparticle structure evolution. *Ex situ* high-energy X-ray diffraction coupled with pair distribution function analysis was employed to obtain detailed information on the atomic-scale ordering, particle phases, structural coherence lengths, and particle segregation. Our studies reveal a spontaneous electrochemically induced formation of PtNi particles of ordered Au_3Cu-type alloy structures from disordered alloy phases (solid solutions) concomitant with surface Ni dissolution, which is coupled to spontaneous residual Ni metal segregation during the activation of $PtNi_6$. Pt-enriched core–shell structures were not formed using the studied Ni-rich nanoparticle precursors. In contrast, disordered $PtNi_3$ alloy nanoparticles lose Ni more rapidly, forming Pt-enriched core–shell structures with superior catalytic activity. Our X-ray scattering results are confirmed by STEM/EELS results on similar nanoparticles.

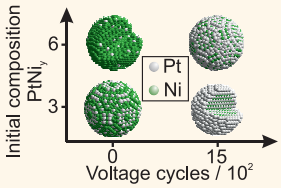

KEYWORDS: PtNi alloys · ASAXS · pair distribution function · fuel cell catalysis · *in situ* characterization

Over the past decade, great research efforts have been directed at the optimization of electrocatalysts for energy conversion. Polymer electrolyte membrane fuel cell (PEMFC) technology is a promising approach for the replacement of fossil fuels with environmental friendly alternatives.[1−8] Fuel cell performance, however, depends strongly on the activity and stability of the catalysts used at the electrodes. Considering the acid environment in a PEMFC, the use of noble metal catalysts, such as Pt nanoparticles, appears indispensable. Platinum, however, is very scarce. One of the solutions to this problem is to reduce the amount of Pt used by alloying it with transition metals.[2,9−20]

Using well-defined model systems Stamenkovic *et al.*[19] showed that the $Pt_3Ni(111)$ crystal surface exhibits 1 order of magnitude higher oxygen reduction reaction (ORR) activity compared to the Pt(111) crystal surface and almost 2 orders of magnitude higher activity compared to commercial Pt nanoparticle (NP) catalysts supported on carbon. Single crystals, however, are not a viable alternative to NP catalysts used in fuel cells.

Recently PtNi NP alloys with >50% Ni content have emerged as an attractive and active bimetallic NP system for achieving both high activity and stability while reducing the amount of Pt used.[21−23] Due to the high initial Ni content, usually the active form of the catalyst is obtained through a Ni dissolution process during an initial NP dealloying step.[24−27] Rudi *et al.*[28] and Wang *et al.*[23] investigated the electrocatalytic activity of Pt_xNi_{1-x} alloys with different initial metal compositions, respectively. The authors demonstrated a significant increase of ORR activity of the bimetallic systems used, as compared to a Pt-based benchmark catalyst. Furthermore, Wang *et al.*[23] and Gan *et al.*[29,30] showed a significant dependence of the structural properties of electrochemically treated binary nanoalloy particles on the initial amount of the non-noble metal in them.

* Address correspondence to x.tuaev@utwente.nl, pstrasser@tu-berlin.de.

Received for review October 30, 2012 and accepted June 27, 2013.

Published online June 27, 2013
10.1021/nn402406k

Similarly, Carpenter *et al.*[21] found a strong morphology change of electrochemically treated Pt_xNi_{1-x} nanoparticles as a function of Pt/Ni reactant ratios. Cui *et al.*[31−33] very recently succeeded in the preparation of a dealloyed octahedral Pt−Ni nanoparticle electrocatalyst, which performed more than tenfold more active for the oxygen reduction reaction than a state-of-art Pt nanoparticle catalyst. STEM analysis showed that the exceptionally active octahedral particles underwent a severe change in morphology toward dealloyed concave Pt−Ni octahedra. On the basis of the results of electrochemical experiments, Hasche *et al.*[34,35] concluded that electrochemical dealloying of homogeneous, Ni-rich, PtNi alloys results in a structural transformation to Pt-enriched nanoparticles concurring with a significantly increased ORR activity. However, knowledge about the time evolution of the structural and compositional changes in NPs during the dealloying step is largely missing.[36,37] In part, this is due to the fact that many of the powerful surface characterization techniques do not provide both atomic-scale resolution and statistical accuracy. For example, a large number of studies have employed transmission electron microscopy (TEM) before and after the NP electrochemical testing.[15,34,38] Although very useful for achieving atomic-level resolution, TEM studies are limited in their statistical accuracy in a sense that only a relatively small number of NPs are analyzed. Statistically more representative results are obtained when a much larger ensemble of NPs is probed, as is the case with X-ray scattering experiments.

In this study we report results from *in situ* and *ex situ* studies on the structural transformations of Ni−Pt alloy NPs under electrochemical *operando* conditions. Using *in situ* anomalous SAXS (ASAXS)[37,39] and *ex situ* high-energy X-ray diffraction (HE-XRD) coupled with atomic pair distribution function (PDF) analysis,[40,46] we observe an unusual structural transformation from chemically disordered to ordered alloy nanophases accompanied by a substantial increase in the catalytic activity. We also observe that the formation of Pt multilayer particle shells[22,23,38,47] is suppressed in NPs with high initial Ni content. The volume-sensitive ASAXS and PDF are powerful methods, but usually used as complementary analytical tools to TEM. Our study shows that synchrotron-based *in situ* and *ex situ* X-ray scattering techniques such as ASAXS and HE-XRD can deliver unparalleled insights into the structure and composition of Pt-based electrocatalysts.

We have synthesized and selected[28] two Pt−Ni alloy NP catalysts, $PtNi_6$ and $PtNi_3$, and studied the structural evolution of their catalytically active dealloyed state using *in situ* ASAXS and *ex situ* HE-XRD-PDF analysis. For each catalyst, we report X-ray scattering-based structural results for the pristine NPs, followed by time-resolved *in situ* ASAXS and *ex situ* PDF structural changes upon electrochemical potential cycling activation.

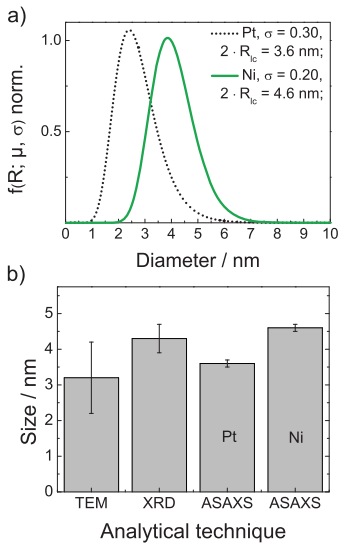

Figure 1. (a) Element-specific mean particle size distribution of pristine $PtNi_6$/Vulcan catalyst: plotted are the best probability density function fits to the Pt (dotted line) and Ni (solid line) edge derived ASAXS profiles, obtained from resonant ASAXS curves for Pt and Ni, respectively. (b) Comparison of mean particle sizes obtained by various techniques employed in this study.

RESULTS AND DISCUSSION

Structural Characterization of Pristine Carbon Supported $PtNi_6$ NPs. *In situ* electrochemical ASAXS experiments were carried out at the 7T-MPW-SAXS beamline at the synchrotron facility BESSY II. We used two different ASAXS data processing methods to extract the resonant terms of scattering: the Stuhrmann method[48,49] and a simplified but very efficient subtraction method.[37,50] A detailed description of the two methods is given in the Supporting Information. Both methods yielded similar results. Particle sizes of Pt−Ni alloys were estimated by collecting data for wave vectors q from 0.35 to 3.5 nm^{-1}. The scattering from the carbon support grains (approximately 100 nm in size) appears at much lower scattering wave vectors q, rendering the simplified subtracting method very reliable.

Anomalous Pt and Ni resonant ASAXS profiles of the pristine $PtNi_6$ NP catalyst (Figure S1a) were found to fit well with a log-normal particle size distribution assuming a spherical particle form factor. Information on NPs sizes was extracted from the estimated element-specific scattering curves by calculating the volume-weighted correlation length diameters ($2R_{lc}$), where $R_{lc} = (2/3)l_c = (2/3)\langle R^4\rangle/\langle R^3\rangle$, R_{lc} is the correlation length radius, and $\langle R^n\rangle$ is the nth moment of the size distribution.[51,52] In contrast to the mean value of a distribution, the correlation length radius R_{lc} represents a more accurate estimate for the NP size, since the latter is directly related to the correlation length l_c, which is a hypothesis-free characteristic constant extractable from ASAXS data without any *a priori* assumptions. Moreover, R_{lc} is the volume-weighted size parameter.

The fits to the experimental scattering curves yielded a characteristic diameter of 4.6 ± 0.1 nm for nickel and 3.6 ± 0.1 nm for platinum species (Figure 1a). These values suggested a strong enrichment of Ni near the surface of the alloy NPs, which is consistent with recent STEM/EELS experiments.[29] This observation did not imply formation of a Ni shell surrounding a PtNi core. Lab-based XRD patterns, shown in Figure S1b, suggest that the pristine NPs represented a chemically homogeneous alloy between Pt and Ni: Broad reflections appeared at Bragg angles between the theoretically estimated positions of the Bragg peaks for pure bulk Pt and Ni. Taking this information into account, a homogeneous alloy with a major amount of Pt atoms distributed near the center of the particle and a minor amount of noble metal near the surface could be assumed. A homogeneous alloy structure was also supported by the HE-XRD experiments, which are introduced and discussed later in the article.

The particle size estimated from the lab-based powder X-ray diffraction patterns using the Scherrer equation[53] is close to 4.3 ± 0.4 nm, which is in good agreement with the estimates of ASAXS. To cross check the SAXS and in-house XRD results, we also conducted TEM experiments (Figure S1c and d). Counting about 200 particles revealed a number-averaged particles size of 3.2 ± 1.0 nm and a volume-averaged particle size of 4.6 ± 1.0 nm. Figure 1b compares the particle size estimates obtained from the various techniques we employed. The differences are due to the different averaging of the different techniques. TEM provides a local particle number-averaged size that is limited by the relatively small number of particles sampled. In contrast, XRD and element-specific ASAXS yield particle-volume-weighted particle sizes.[52,54]

Structural Evolution of $PtNi_6$ NPs during Activation, Catalysis and Potential Cycling. We investigated the structural changes of $PtNi_6$ NPs during an extensive electrochemical potential cycling protocol involving activation, ORR catalysis, and stability testing using *in situ* ASAXS in liquid electrolyte. Figure 2a shows the time evolution of the mean element-specific Pt edge and Ni edge derived particle sizes as a function of the number of potential cycles (scattering curves are shown in Figure S2). Overall, Pt and Ni size distributions show only moderate changes during potential cycling. Exposure of $PtNi_6$ alloy nanoparticles to acidic electrolyte leads to a spontaneous dissolution of the low-coordinated Ni atoms on the surface of particles, as indicated by a Ni size distribution decreasing from 4.6 ± 0.1 nm (pristine powder) to 3.9 ± 0.1 nm (0 CV, *in situ* ASAXS). In contrast, the size distribution of the noble metal, Pt, remains unchanged (3.6 ± 0.1 nm for pristine powder and 3.6 ± 0.1 nm in the case of 0 CV, *in situ* ASAXS).

Potential cycling induced a Pt size distribution increase from an initial value of 3.6 ± 0.1 nm to 3.8 ± 0.1 nm. Over the first 500 cycles, however, the mean Ni size distribution first dropped from 3.9 ± 0.1 nm to 3.6 ± 0.1 nm and then increased to 4.0 ± 0.1 nm, indicating rapid initial Ni surface dissolution followed by subsequent lattice expansion due to the structural transformation from a Ni-rich solid solution to a Pt-enriched Pt–Ni alloy phase with at least partial atomic ordering. This hypothesis is confirmed by HE-XRD results discussed below. One of the key conclusions from the comparison of the two mean element-specific size distributions is that throughout the electrochemical cycling and the concurrent loss of Ni, counterintuitively, the particles did not form Pt-enriched shells of any significant thickness. This implies that Pt atoms initially dissolved in a Ni matrix rearrange and form a more homogeneous structure during the dealloying process. This is in line with a recent STEM/EELS study of the dealloying behavior of Ni-rich Pt:Ni 1:5 alloy nanoparticles.[29]

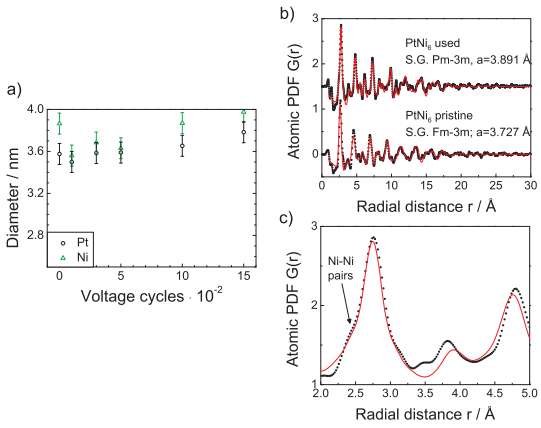

Figure 2. (a) Element-specific mean particle size evolution during electrode potential cycling of the $PtNi_6$ catalyst, measured using *in situ* ASAXS, Pt-edge-derived mean size (black circles), and Ni-edge-derived mean size (green triangles). (b) Experimental (black dots) and model fit atomic PDFs (red lines) for pristine (bottom) and cycled/dealloyed (top) $PtNi_6$. Space group (S.G.) and unit cell parameters of the model PDFs are provided for each data set. (c) Blown-up low-*r* part of the atomic PDF data of the dealloyed $PtNi_6$ catalyst showing the presence of a low-*r* feature in the first PDF peak that could be identified with the presence of Ni–Ni bonds from Ni-rich domains. The PDF model (red line) features a chemically ordered (S.G. *Pm*-3*m*) cubic lattice.

We investigated the structural changes of the $PtNi_6$ nanoalloys using *ex situ* high-energy XRD experiments coupled with an atomic PDF analysis of pristine and electrochemically cycled samples. Atomic PDF analysis has proven to be a very powerful tool for structural characterization of NPs, yet has rarely been applied in the realm of Pt alloy fuel cell catalyst research.

HE-XRD experiments were carried out on Pt–Ni NP samples supported on carbon paper. The experiments were done at the beamline 11-ID-C at the Advanced Photon Source, Argonne, using X-rays of energy 115 keV (wavelength λ = 0.1080 Å). The use of higher energy X-rays allows collecting data to higher wave vectors, which is crucial for obtaining good-quality atomic PDFs. With the present experiments XRD data

up to wave vectors of 28 Å^{-1} were collected. The XRD data were reduced to atomic PDFs, shown in Figure 2b,c. The PDF of the fresh $PtNi_6$ particles is well approximated with a model based on the face centered cubic (fcc) lattice of Ni, where some Pt atoms are accommodated in a random manner, resulting in a chemically disordered, solid solution type single nanophase.

HE-XRD pattern of the dealloyed $PtNi_6$ catalyst shows a clear shift of Bragg peaks toward smaller angles, which evidence an increase in the lattice parameter due to Ni dissolution (Figure S3). The experimental PDFs $G(r)$ of the pristine and dealloyed Pt−Ni catalysts are shown in Figure 2b at bottom and top, respectively. They were fit with models featuring a chemically disordered (*e.g.*, solid solution of Ni and Pt) fcc-type structure as well as with a chemically ordered cubic $CuAu_3$-type structure (red lines). The pristine PDF is consistent with a Pt−Ni solid solution structure, while the atomic PDF for the dealloyed catalyst is well fit using a chemically ordered cubic-type structure. A surprising finding is that $G(r)$ of the dealloyed catalysts reveals a characteristic shoulder on the low r side of the first major PDF peak (see Figure 2c), which is consistent with Ni−Ni bond lengths suggesting an appearance of Ni-rich domains.

Our HE-XRD and PDF analysis suggests that Pt and nondissolved Ni atoms inside the particles rearrange from a disordered solid-solution phase into an chemically ordered alloy phase in the course of the potential cycling and Ni dissolution. To the best of our knowledge, that is the first report on an electrochemically induced chemical ordering of bimetallic NPs. As the experimental data indicate, inside the particles, pure Ni domains are very likely to have formed, due to Ni segregation triggered by the dissolution and atomic rearrangement catalytic processes.

In order to quantify the elemental composition change during potential cycling, we performed X-ray fluorescence (XRF) analysis on the as-obtained and electrochemically tested catalysts (see Figure S4a). The pristine NPs are rich in Ni and with a composition of $Pt_{14}Ni_{86}$ (equivalent to $PtNi_6$), evolving under electrochemical cycling into Pt-rich NPs with a composition of $Pt_{76}Ni_{23}$ (equivalent to Pt_3Ni). We note that Vegard's rule is not followed well by the pristine Pt−Ni NPs despite their chemically disordered (solid solution) structure. The chemically disordered alloy model derived unit cell parameter of 3.727 Å in Figure 2b thus suggests a not completely random alloying in the pristine NPs, which may well explain the ease with which they transform into chemically ordered NPs when subjected to catalytic reactions.

In summary, we have found evidence that not completely random yet chemically disordered Pt−Ni alloy NPs spontaneously transform into an ordered Au_3Cu type Pt−Ni alloy phase upon electrochemical dissolution of Ni. This, to the best of our knowledge, is the first time such an electrochemically induced atomic ordering has been observed. Although Ni dissolved in a large amount, some residual Ni atoms formed domains coexisting with the ordered Pt−Ni alloy phase.

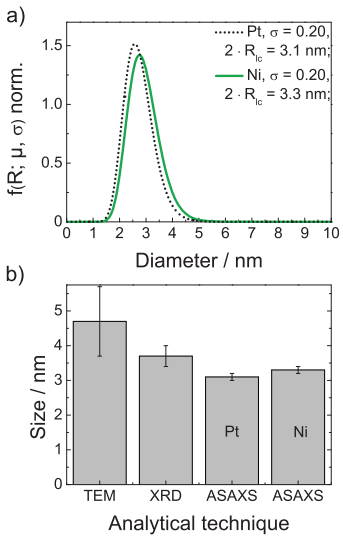

Figure 3. Size characterization of a pristine $PtNi_3$/Vulcan catalyst: (a) probability density functions of the NP size, obtained from resonant ASAXS curves for Pt (dotted line) and Ni (solid line) species, respectively. (b) Comparison of particle size estimates obtained by three different techniques used in the present study.

Structural Characterization of Pristine Carbon Supported $PtNi_3$ NPs. We selected carbon-supported $PtNi_3$ as the second NP catalyst for our structural studies. This catalyst showed high initial catalytic ORR activity, which was further enhanced by electrochemical potential cycling.[28]

$PtNi_3$/Vulcan catalyst was studied first as pristine material. Anomalous Pt and Ni resonant ASAXS profiles of the pristine $PtNi_3$ NP catalyst (Figure S5a) were fitted with a log-normal particle size distribution assuming a spherical particle form factor. The particle size probability density function was extracted from the experimental ASAXS data. The ASAXS-estimated particle size, based on correlation lengths, is 3.1 ± 0.1 nm for Pt and 3.3 ± 0.1 nm for Ni species (see Figure 3a). Analysis of the in-house XRD patterns yielded a particle size of 3.7 ± 0.3 nm (experimental data are shown in Figure S5b), in good accord with the ASAXS results.

Again, the in-house XRD patterns exhibit broad Bragg peaks that are positioned between the peaks seen with pure bulk Pt and Ni. Hence, single alloy particles are expected for the as-obtained $PtNi_3$/C sample. Particle size estimated from TEM images (shown in Figure S5c) showed a log-normal size distribution (Figure S5d) centered at about 4.7 ± 0.8 nm (number average) and a volume average mean size of 5.1 ± 1.0 nm. Figure 3b shows a comparison between the size estimates obtained by the three different techniques employed here. Again, particle sizes estimated by TEM deviate most from those determined with the statistically more representative XRD and ASAXS techniques.

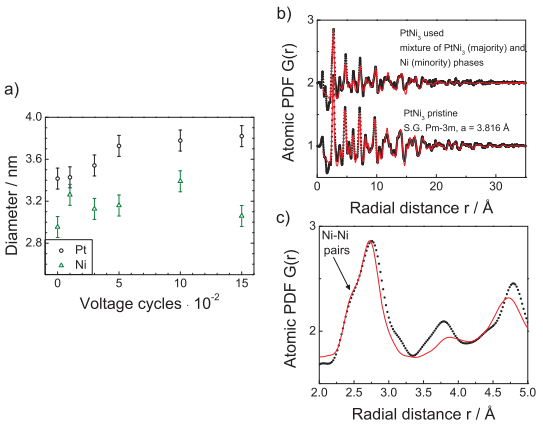

Figure 4. (a) Element-specific mean particle size evolution during electrode potential cycling of the $PtNi_3$ catalyst, measured using *in situ* ASAXS, Pt-edge-derived mean size (black circles), and Ni-edge-derived mean size (green triangles). In (b) experimental (dots) and model atomic PDFs (lines) for pristine and used $PtNi_3$ are shown, while (c) shows the low-*r* part of the atomic PDFs. The PDF models feature chemically ordered (*Pm*-3*m*) and disordered (*Fm*$\bar{3}$*m*) cubic-type phases for the fresh and used NPs, respectively.

Structural Evolution of $PtNi_3$ NP Catalyst during Activation, Catalysis, and Potential Cycling. Applying the same electrochemical potential stress protocol tests as for $PtNi_6$/Vulcan catalyst, the structural evolution of $PtNi_3$ alloy NPs was also studied. A clear difference when compared to the case of $PtNi_6$ can be seen in the *in situ* ASAXS data of $PtNi_3$ catalyst (Figure 4a, experimental data are shown in Figure S6). The difference is in the trend of the resonant correlation length diameters. Here both Pt and Ni species' diameters increase over the first 1000 potential cycles. The Pt size increased from an initial value of 3.4 ± 0.1 nm to 3.8 ± 0.1 nm. The Ni size increased over the first 1000 cycles from 3.0 ± 0.1 nm to 3.5 ± 0.1 nm. However, during an additional 500 cycles the Ni size decreased to a final value of 3.1 ± 0.1 nm. The Pt and Ni diameters, however, differ, indicating that the Pt and transition metals (Ni) species rearrange somewhat differently within the NPs during ORR reaction.

To obtain a better insight in the structural rearrangement in $PtNi_3$ NPs caused by the electrochemical treatment, we probed both fresh and used $PtNi_3$ samples with high-energy XRD coupled to atomic PDF analysis. The respective atomic PDFs are shown in Figure 4b. That of fresh $PtNi_3$ particles may be well approximated with a single-phase model based on the archetypal, chemically ordered $AuCu_3$-type structure. The PDF of the used $PtNi_3$ particles may be explained only in terms of a mixture of two nanophases. We see a clear signature of plenty of Ni–Ni distances (Figure 4c). These are not seen as much in the fresh sample, which, therefore, may be called a typical chemically ordered alloy. The observation of an excess of Ni–Ni bonds in the used $PtNi_3$ is a clear signature of dealloying or phase segregation.

Taking into account the ASAXS-determined NPs' diameters, the PDF findings for the $PtNi_3$ catalyst may be rationalized in terms of a rearrangement of initially chemically homogeneous alloy NPs to NPs with a core–shell structure. Here Ni atoms do not leach out of the particle completely since the thickness of Pt on the particle surface increases. This is consistent with the formation of a PtNi-core/Pt-shell structure of the treated catalyst.

Similar structural evolution of $PtNi_3$ alloy nanoparticles, which were studied before and after electrochemical dealloying, was observed in a recently published study of Gan *et al.*[29] The results based on a STEM/EELS study suggest a formation of Pt-rich shells surrounding PtNi cores. A remarkable finding was that the particles with an initial composition of $PtNi_3$ do not behave as predicted by a simple dealloying model, where the Ni concentration shows a monotonic decrease of concentration from the center to the surface of the particle. Gan *et al.* observe an unusual Ni composition profile across the core, where an enrichment of Ni atoms near the surface appeared.[29] According to these results, our particles with similar initial Ni content show an enrichment of the NPs shell with Ni atoms during the first 1000 potential cycles, as indicated by the increase of Ni diameter ASAXS data. Subsequently, dissolution of Ni from this area remains the predominant intraparticle structural process. The results are in full agreement with previous studies on PtCu and PtCo alloy nanoparticles.[24,38,55]

Furthermore, we estimated the element composition of fresh $PtNi_3$ and electrochemically treated alloy nanoparticles by XRF. The XRF data show an evolution of the pristine $Pt_{27}Ni_{73}$ alloy catalyst to a Pt-rich $Pt_{73}Ni_{27}$ alloy (Figure S4b). We compared our findings with a model suggested by Wang *et al.*[23] The model data, which include an experimentally estimated value for an initially chemically homogeneous $Pt_{25}Ni_{75}$ alloy, reveals the formation of a Pt-rich $Pt_{87}Ni_{13}$ catalyst. In this study a PtNi-core/Pt-shell structure with a shell thickness of >1 nm was deduced from experimental data and supported by calculations. Our data show a similar tendency for a PtNi-core/Pt-shell structure formation. Additionally we find a shell thickness of approximately 1 nm, according to a comparison of the estimated sizes of electrochemically treated $PtNi_3$ particles.

Nanoparticle Structure, Composition, and Catalytic Activity. On the basis of the experimental mean particle size evolution for $PtNi_6$ and $PtNi_3$ NPs, we have obtained an improved understanding of the structural transformations of Pt–Ni alloy NPs under electrochemical conditions. Table 1 summarizes the most significant experimental results, and the scheme presented in Figure 5 illustrates our new insights based on these values.

$PtNi_6$ alloy NPs are characterized by Pt atoms dissolved in a Ni matrix (solid solution); see Figure 5a. Exposure of Ni to acid electrolyte leads to a spontaneous dissolution of surface Ni atoms. Subsequent electrochemical cycling leads to Ni surface dissolution

TABLE 1. Summary of the Experimental Findings for Pristine and Potential Protocol Exposed PtNi Alloy Nanoparticles

	$PtNi_6$ pristine powder	$PtNi_3$ pristine powder
ASAXS Pt	3.6 ± 0.1 nm	3.1 ± 0.1 nm
ASAXS Ni	4.6 ± 0.1 nm	3.3 ± 0.1 nm
XRD	4.3 ± 0.4 nm, homogeneous alloy	3.7 ± 0.3 nm, homogeneous alloy
TEM num.-av (vol.-av)	3.2 ± 1.0 (4.6 ± 1.0) nm	4.7 ± 1.0 (5.1 ± 1.0) nm

	$PtNi_6$ treatment		$PtNi_3$ treatment	
	fresh	treated	fresh	treated
in situ ASAXS Pt	3.6 ± 0.1 nm	3.8 ± 0.1 nm	3.4 ± 0.1 nm	3.8 ± 0.1 nm nm
in situ ASAXS Ni	3.9 ± 0.1 nm	4.0 ± 0.1 nm	3.0 ± 0.1 nm	3.1 ± 0.1 nm
HE-XRD/PDF	fcc lattice of Ni with randomly accommodated Pt atoms	ordered Pt_3Ni (Au_3Cu-type) particles with Ni-rich domains	archetypal, chemically ordered $PtNi_3$ alloy	mixture of $PtNi_3$ (majority) and Ni (minority) phases

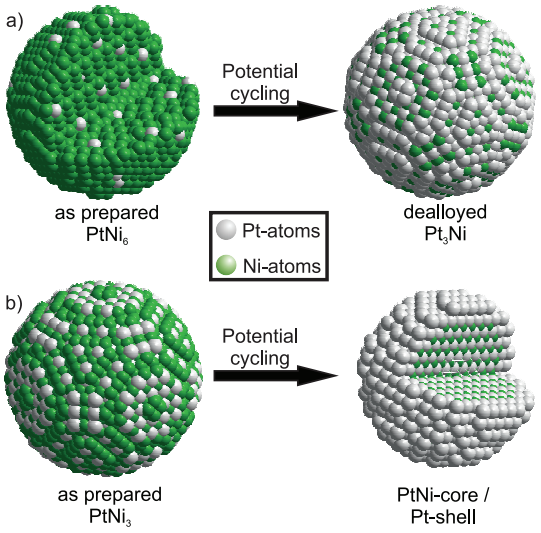

Figure 5. Schematic representation of Pt–Ni alloy nanoparticle evolution during electrocatalysis (a) for $PtNi_6$/Vulcan catalyst and (b) for $PtNi_3$/Vulcan.

and a rapid rearrangement of Pt and residual Ni atoms until an ordered Au_3Cu alloy structure type is formed. ASAXS data confirmed that throughout the electrochemical cycling Ni atoms remained fairly uniformly distributed across the bulk of the NPs, keeping Pt surface enrichments and Pt shell formations insignificant.

On the other hand, the electrochemical treatment of pristine disordered $PtNi_3$ alloy NPs promoted rapid Ni surface dissolution yielding clear PtNi-core/Pt-shell-type NPs of slightly smaller size, Figure 5b. The resulting phase-segregated Ni domains appear dispersed within the core–shell NPs (not shown).

Compositional variations of the Ni-rich Pt–Ni NPs toward Pt-rich NPs are in general agreement with earlier findings by Wang *et al.*[42] and Gan *et al.*[29] However, in addition, our X-ray-based results provide time-evolution insight into the elemental redistribution, revealing an unexpected electrochemically induced metal ordering in NPs of high initial Ni content.

Electrocatalytic activity for the reduction of molecular oxygen on dealloyed Pt–Ni NPs is closely tied to the details of the surface and near surface structure of the leached NPs. Enhanced catalytic ORR activity was observed for porous,[22,57] core–shell[10,15,18,24,34,55] and so-called skeleton structures.[21,23,38] ORR activity values of the materials considered here were reported elsewhere.[28] They confirm the findings of Gan *et al.*[29] that dealloyed $PtNi_3$ core–shell NPs outperform leached $PtNi_6$ NPs with a negligibly small Pt-enriched shell.

Our study reveals never before reported structure evolution in Pt–Ni NP catalysts caused by electrochemical potential cycling. The accuracy of our results is enhanced by the usage of *in situ* and *ex situ* X-ray scattering techniques capable of sampling a large amount of NPs. Taking into account previous studies,[57,58] the increasing ORR activity from NPs with $PtNi_6$ composition to NPs with $PtNi_3$ composition can be explained in terms of a structural rearrangement process as follows: The electrochemical treatment of Ni-rich Pt–Ni alloy catalyst first leads to a chemically ordered alloy structure and then enriches the NP surface with Pt species. The resulting NPs with Pt-enriched surface also have compressed Pt–Pt interatomic distances due to the underlying PtNi core.

CONCLUSIONS

We have investigated the chemical and atomic-scale structural evolution of two Pt–Ni NP fuel cell catalysts under electrochemical potential cycling conditions using *in situ* ASAXS and *ex situ* HE-XRD/PDF techniques. These scattering techniques are complementary to TEM-based real-space imaging methods and provide unparalleled structural information with high statistical accuracy.

Our results offer a clearer picture of how the NPs evolve during the electrochemical activation and catalysis. In pristine disordered $PtNi_6$ alloy catalyst NPs, Pt atoms are statistically distributed inside a face-centered cubic matrix of Ni atoms. During electrochemical activation cycling, Ni surface atoms selectively leach from the NPs, yet remain uniformly distributed thanks to the large-scale Pt and Ni atom rearrangement.

Surprisingly, Pt and residual bulk Ni atoms rearrange and form a chemically ordered Au_3Cu-type Pt-rich alloy phase. In contrast, disordered $PtNi_3$ catalyst NPs leach Ni more rapidly and evolve into PtNi-core/Pt-shell NP structures, where compressive surface strain effects are responsible for their higher catalytic activity.

EXPERIMENTAL METHODS

Synthesis of $PtNi_6$/Vulcan and $PtNi_3$/Vulcan Catalysts. Details on particle synthesis and electrochemical characterization are described in our previous work.[28] A polyol method, previously described in the literature,[9] was chosen to prepare PtNi alloy nanoparticles. In 100 mL three-neck flasks, equipped with a reflux cooler, 0.3 mmol of $Ni(ac)_2 \cdot 4H_2O$ (99.998%, Sigma Aldrich), 0.4 mmol of 1,2-tetradecanediol (90%, Sigma Aldrich), 0.3 mL of oleylamine (70%, Sigma Aldrich), and 0.3 mL of oleic acid (99%, Alfa Aesar) were added to 25 mL of diphenyl ether (99%, Alfa Aesar). The reaction mixture was stirred for 5 min under a nitrogen atmosphere, followed by raising the temperature to 80 °C. After about 30 min, the temperature was raised to 200 °C. At this temperature, 0.1 mmol of $Pt(acac)_2$ (min. 48% Pt, Alfa Aesar) dissolved in 1.5 mL of 1,2-dichlorobenzene (>99%, Alfa Aesar) was added, and the reaction mixture was stirred at 200 °C for 1 h. Subsequently, the reaction mixture was cooled to room temperature; 5 mL of dichloromethane (99.8%, Merck) and 20 mL of ethanol were added to the cooled reaction mixture. Separately, 78.1 mg of Vulcan XC 72R was mixed with 40 mL of toluene and was dispersed in an ultrasonic bath for 10 min. This suspension was added to the reaction mixture and was stirred for 24 h at room temperature. The product was centrifuged and washed three to four times with ethanol, followed by drying in a freeze-dryer. The dried catalyst was heated in a furnace in a N_2 atmosphere at 230 °C and was held there for 4 h to remove surfactants and enhance the atomic mixing of Ni and Pt.

Transmission Electron Microscopy. For TEM sample preparation a small amount of the synthesized powder was dispersed *via* ultrasonication in 0.5 mL of ^{i}PrOH. A Cu grid with holey carbon film was impregnated with 2 μL of the solution and air-dried. TEM measurements were conducted using a FEI TECNAI G^2 20 S-TWIN microscope, equipped with a GATAN MS794 P CCD detector, which was operated by the accelerating voltage of 200 kV. TEM images were evaluated using ImageJ software.[54] Histograms were produced from counting 200 particles and fitted with a log-normal particle size distribution. The reported values of mean particle size and standard deviation were extracted from the fit.

Anomalous Small-Angle X-ray Scattering. Anomalous small-angle X-ray scattering experiments were performed *in situ* at the Berlin synchrotron facility BESSY II, operated by the Helmholtz Zentrum Berlin, at the 7T-MWP-SAXS beamline. Data were collected with a CCD of type MAR165 (Rayonix) using X-rays of energies 11 490 and 11 560 eV below the Pt-L_{III} absorption edge and X-rays of energies 8101 and 8330 eV below the Ni-K edge, during an electrochemical treatment described in Table 2. For the electrochemical treatment a catalyst powder suspension/ink was prepared, as described in the literature.[28] In particular, a defined amount of the PtNi catalyst powder (5−6 mg) was dispersed in a mixture of 2.490 mL of unltrapure water (Millipore), 2.490 mL of ^{i}PrOH, and 0.020 mL of a 5 wt % isopropanolic Nafion solution. A carbon paper sheet was covered 10 times with 10 μL of the ink, respectively. The as-prepared working electrode, a Pt-wire counter electrode, and a 3 M Ag/AgCl reference electrodes were placed in an *in situ* electrochemical cell (Figure S7),[37] which was filled with 0.1 M $HClO_4$. Electrochemical potential control was carried out using a Gamry ref-600 potentiostat. Scattering curves were collected *in situ* and subsequently corrected for transmission and background. Fitting the experimental data was performed with SASfit 0.93.2,[55] assuming a logarithmic normal distribution of hard spheres. A detailed description of fitting is reported elsewhere.[56]

Data processing known as the Stuhrmann method is based on calculations published by Stuhrmann *et al.*[44] The authors consider a mathematical relationship for several scattering curves obtained at different energies to extract the element of interest resonant term of scattering. As reported in the literature, an essential equation for this purpose is

$$I(q;E_i) = I_0(q) + 2f'(E_i)\, I_{0r}(q) + [(f'(E_i)^2 + (f''(E_i))^2]I_r(q) \quad (2)$$

Here $I_0(q)$ is the nonresonant part of the scattering data, $I_r(q)$ is the resonant part, $I_{0r}(q)$ is the cross term of the resonant and nonresonant scattering, and $f'(E_i)$ and $f''(E_i)$ are the scattering factors at the energy E_i. In the Supporting Information we report on the comparison of the ASAXS data analysis using the Stuhrmann method (eq 2) and a simplified subtraction method (eq 3) inspired by Haubold *et al.*[45] The second method was used here for determination of resonant scattering curves. It is based on the following equation:

$$I_{resonant}(q) = I(q;E_2) - I(q;E_1);\ E_1 > E_2 \quad (3)$$

In the our study ASAXS results obtained from the subtraction method are discussed.

TABLE 2. Detailed Electrochemical Treatment of PtNi Nanoparticles Supported on Vulcan for Structural *in Situ* Characterization with ASAXS[a]

no. of technique[b]	technique	no. of cycles	potential range [V]	scan rate [mV/s]	no. of loops
1	ASAXS/CA		0.50		
2	CV	3	0.05−1.10	50	
3	ASAXS/CA		0.50		
4	activation-CV	200	0.05−1.10	500	
5	ASAXS/CA		0.05		
6+*n*	AST-CV	100	0.50−1.10	50	24
7+*n*	ASAXS/CA		0.50		24

[a] Electrochemical techniques are abbreviated as CA (chronoamperommetry), CV (cyclic voltammetry), AST-CV (acceleration stress test potential cycles). [b] $n = 2, 4, 6, 8, 10, 12, 14, 16, 18, 20, 22, 24$.

High-Energy X-ray Diffraction Measurements. High-energy XRD measurements were performed at the beamline 11-ID-C, at the Advanced Photon Source, Argonne, using X-rays of energy 115 keV (λ = 0.1080 Å). Inks of the catalysts were dropped on carbon paper and so subjected to the XRD measurements in transmission geometry, with the inks facing the detector. The XRD data were reduced to the so-called structure factors, $S(q)$, and then Fourier transformed to the corresponding atomic PDFs $G(r)$, using the relationship

$$G(r) = \frac{2}{\pi}\int_{q=0}^{q_{max}} q[S(q) - 1]\sin(qr)\, dq \quad (1)$$

where q_{max} = 28 Å^{-1} in the present experiments. The wave vector q is defined as $q = 4\pi\sin(\theta)/\lambda$, where θ is half of the scattering angle and λ is the wavelength of the X-rays used. The structure function $S(q)$ is related to only the coherent part of the scattered X-ray intensities. Note, as derived, atomic PDFs $G(r)$ are experimental quantities that oscillate around zero and show positive peaks at real-space distances, r, where the local atomic density $\rho(r)$ exceeds the average one, ρ_o. This behavior can be expressed by the equation $G(r) = 4\pi r\rho_o[\rho(r)/\rho_o - 1]$, which is the formal definition of the PDF $G(r)$. High-energy XRD and atomic PDFs have already proven to be very efficient in studying the atomic-scale structure of nanosized materials,[40] including chemical order−disorder effects.[41,57]

Modeling Details. The experimental PDFs were fit with structure models based on chemically disordered (S.G. $Fm\bar{3}m$) and chemically ordered (S.G. Pm-3m) cubic-type atomic structures exhibited by noble−transition metal alloys. In this type of Bravais lattices based modeling a PDF for an infinite cubic lattice is first computed. Then each of the coordination spheres of the perfect lattice is broadened by a convolution with a Gaussian function to take into account the presence of thermal and static local atomic displacements in real nanoparticles. At the same time the computed PDF is multiplied by a particle shape (spherical in our case)-dependent function, which is zero for distances longer than the size of the nanoparticles being modeled. It is a simplistic approximation to the structure of real NPs but is useful since it allows (i) to verify their type of atomic ordering and (ii) obtain a set of structural parameters (*e.g.*, lattice constants and atomic displacement amplitudes) that may be compared directly with those for the corresponding bulk materials. The computations were done with the help of the program PDFgui.[58]

X-ray Fluorescence Measurements. XRF spectra were collected using a Bruker Tornado M4 spectrometer. X-ray source emitting Cu Kα radiation was operated at 35 kV, 800 μA. Fresh and electrochemically treated (ASAXS study postmortem electrodes) were irradiated under vacuum (19 mbar) with an X-ray beam spot size of 22 μm. Each presented spectrum is a mean average of 10 measurements with an acquisition time of 10 s each. Element composition was determined in atomic % by integrating Pt and Ni resonant fluorescence peaks.

Conflict of Interest: The authors declare no competing financial interest.

Supporting Information Available: Experimental data on pristine powder characterization, as well as a comparison of the ASAXS data processing Stuhrmann method and subtraction method are provided. This material is available free of charge *via* the Internet at http://pubs.acs.org.

Acknowledgment. We thank Dipl.-Phys. L. Anklamm and Dr. W. Malzer from the Berlin Laboratory for Innovative X-ray Technologies (BLiX), Dipl.-Phys. R. Erler from Bruker Nano GmbH, and Prof. Dr. G. Mul from the Universiteit Twente for fruitful scientific discussions. This work was supported by the Cluster of Excellence in Catalysis (UNICAT) funded by the German National Science Foundation (DFG) and managed by the Technische Universitaet Berlin. Portions of this research were carried out at BESSY II, a national user synchrotron facility operated by the Helmholtz-Zentrum Berlin. Part of the work done by V.P. was supported by DOF Grant DE-SC0006877. Work at APS is supported by the DOE under Contract DE-AC02-06CH11357.

REFERENCES AND NOTES

1. Borup, R. L.; Davey, J. R.; Garzon, F. H.; Wood, D. L.; Inbody, M. A. PEM Fuel Cell Electrocatalyst Durability Measurements. *J. Power Sources* **2006**, *163*, 76–81.
2. Hasché, F.; Oezaslan, M.; Strasser, P. Activity, Stability and Degradation of Multi Walled Carbon Nanotube (MWCNT) Supported Pt Fuel Cell Electrocatalysts. *Phys. Chem. Chem. Phys.* **2010**, *12*, 15251–15258.
3. He, C.; Desai, S.; Brown, G.; Bollepalli, S. PEM Fuel Cell Catalysts: Cost, Performance, and Durability. *Electrochem. Soc. Interface* **2005**, 41–44.
4. Ofstad, A. B.; Thomassen, M. S.; de la Fuente, J. L. G.; Seland, F.; Moller-Holst, S.; Sunde, S. Assessment of Platinum Dissolution from a Pt/C Fuel Cell Catalyst: An Electrochemical Quartz Crystal Microbalance Study. *J. Electrochem. Soc.* **2010**, *157*, B621–B627.
5. Rinaldo, S. G.; Stumper, J.; Eikerling, M. Physical Theory of Platinum Nanoparticle Dissolution in Polymer Electrolyte Fuel Cells. *J. Phys. Chem. C* **2010**, *114*, 5773–5785.
6. Wagner, F. T.; Yan, S. G. Catalyst and Catalyst-Support Durability. In *Handbook of Fuel Cells - Fundamentals, Technology and Applications*; Vielstich, W.; H, Y.; Gasteiger, H. A., Eds.; John Wiley & Sons, Ltd.: 2009; Vol. 5, pp 250−263.
7. Yuan, H. P.; Song, H. Q.; Qiu, X. P.; Zhu, W. T.; Chen, L. Q. Electrochemical Characters and Structure Changes of Electrochemically Treated Pt Nanoparticles. *Electrochem. Commun.* **2010**, *12*, 14–17.
8. Zhang, S. S.; Yuan, X. Z.; Hin, J. N. C.; Wang, H. J.; Friedrich, K. A.; Schulze, M. A Review of Platinum-Based Catalyst Layer Degradation in Proton Exchange Membrane Fuel Cells. *J. Power Sources* **2009**, *194*, 588–600.
9. Ahrenstorf, K.; Albrecht, O.; Heller, H.; Kornowski, A.; Gorlitz, D.; Weller, H. Colloidal Synthesis of Ni_xPt_{1-x} Nanoparticles with Tuneable Composition and Size. *Small* **2007**, *3*, 271–274.
10. Hasché, F.; Oezaslan, M.; Strasser, P. Activity, Stability, and Degradation Mechanisms of Dealloyed $PtCu_3$ and $PtCo_3$ Nanoparticle Fuel Cell Catalysts. *ChemCatChem* **2011**, *3*, 1805–1813.
11. Ahrenstorf, K.; Heller, H.; Kornowski, A.; Broekaert, J. A. C.; Weller, H. Nucleation and Growth Mechanism of Ni_xPt_{1-x} Nanoparticles. *Adv. Funct. Mater.* **2008**, *18*, 3850–3856.
12. Cui, C. H.; Li, H. H.; Yu, S. H. Large Scale Restructuring of Porous Pt-Ni Nanoparticle Tubes for Methanol Oxidation: A Highly Reactive, Stable, and Restorable Fuel Cell Catalyst. *Chem. Sci* **2011**, *2*, 1611–1614.
13. Debe, M. K.; *et al*. Extraordinary Oxygen Reduction Activity of Pt_3Ni_7. *J. Electrochem. Soc.* **2011**, *158*, B910–B918.
14. Du, C.; Chen, M.; Wang, W.; Yin, G. Nanoporous PdNi Alloy Nanowires as Highly Active Catalysts for the Electro-Oxidation of Formic Acid. *ACS Appl. Mater. Interfaces* **2011**, *3*, 105–109.
15. Gan, L.; Yu, R.; Luo, J.; Cheng, Z.; Zhu, J. Lattice Strain Distributions in Individual Dealloyed Pt-Fe Catalyst Nanoparticles. *J. Phys. Chem. Lett.* **2012**, *3*, 934–938.
16. Gasteiger, H. A.; Kocha, S. S.; Sompalli, B.; Wagner, F. T. Activity Benchmarks and Requirements for Pt, Pt-Alloy, and Non-Pt Oxygen Reduction Catalysts for PEMFCs. *Appl. Catal., B* **2005**, *56*, 9–35.
17. Koh, S.; Strasser, P. Electrocatalysis on Bimetallic Surfaces: Modifying Catalytic Reactivity for Oxygen Reduction by Voltammetric Surface De-Alloying. *J. Am. Chem. Soc.* **2007**, *129*, 12624–12625.
18. Oezaslan, M.; Strasser, P. Activity of Dealloyed $PtCo_3$ and $PtCu_3$ Nanoparticle Electrocatalyst for Oxygen Reduction Reaction in Polymer Electrolyte Membrane Fuel Cell. *J. Power Sources* **2011**, *196*, 5240–5249.
19. Stamenkovic, V. R.; Fowler, B.; Mun, B. S.; Wang, G. F.; Ross, P. N.; Lucas, C. A.; Markovic, N. M. Improved Oxygen Reduction Activity on $Pt_3Ni(111)$ *via* Increased Surface Site Availability. *Science* **2007**, *315*, 493–497.
20. Yano, H.; Kataoka, M.; Yamashita, H.; Uchida, H.; Watanabe, M. Oxygen Reduction Activity of Carbon-Supported Pt-M (M = V, Ni, Cr, Co, and Fe) Alloys Prepared by Nanocapsule Method. *Langmuir* **2007**, *23*, 6438–6445.
21. Carpenter, M. K.; Moylan, T. E.; Kukreja, R. S.; Atwan, M. H.; Tessema, M. M. Solvothermal Synthesis of Platinum Alloy Nanoparticles for Oxygen Reduction Electrocatalysis. *J. Am. Chem. Soc.* **2012**, *134*, 8535–8542.
22. Snyder, J.; McCue, I.; Livi, K.; Erlebacher, J. Structure/Processing/Properties Relationships in Nanoporous Nanoparticles as Applied to Catalysis of the Cathodic Oxygen Reduction Reaction. *J. Am. Chem. Soc.* **2012**, *134*, 8633–8645.
23. Wang, C.; *et al*. Correlation between Surface Chemistry and Electrocatalytic Properties of Monodisperse Pt_xNi_{1-x} Nanoparticles. *Adv. Funct. Mater.* **2011**, *21*, 147–152.
24. Strasser, P.; *et al*. Lattice-Strain Control of the Activity in Dealloyed Core-Shell Fuel Cell Catalysts. *Nat. Chem.* **2010**, *2*, 454–460.
25. Strasser, P. Dealloyed Pt Bimetallic Electrocatalysts for Oxygen Reduction. In *Handbook of Fuel Cells: Advances in Electrocatalysis, Materials, Diagnostics and Durability*; Vielstich, W.; Gasteiger, H. A.; Yokokawa, H., Eds.; John Wiley & Sons Ltd: Chichester, West Sussex, UK, 2009; Vols. 5 and 6, pp 30−47.
26. Strasser, P. Dealloyed Core Shell Fuel Cell Electrocatalysts. *Rev. Chem. Eng.* **2009**, *25*, 255–295.

27. Liu, Z.; Yu, C.; Rusakova, I.; Huang, D.; Strasser, P. Synthesis of Pt_3Co Alloy Nanocatalyst *via* Reverse Micelle for Oxygen Reduction Reaction in PEMFCs. *Top. Catal.* **2008**, *49*, 241–250.
28. Rudi, S.; Tuaev, X.; Strasser, P. Electrocatalytic Oxygen Reduction on Dealloyed $Pt_{1-x}Ni_x$ Alloy Nanoparticle Electrocatalysts. *Electrocatalysis* **2012**, *3*, 265–273.
29. Gan, L.; Heggen, M.; Rudi, S.; Strasser, P. Core-Shell Compositional Fine Structures of Dealloyed Pt_xNi_{1-x} Nanoparticles and Their Impact on Oxygen Reduction Catalysis. *Nano Lett.* **2012**, *12*, 5423–5430.
30. Gan, L.; Heggen, M.; O'Malley, R.; Theobald, B.; Strasser, P. Understanding and Controlling Nanoporosity Formation for Improving the Stability of Bimetallic Fuel Cell Catalysts. *Nano Lett.* **2013**, *13*, 1131–1138.
31. Cui, C.; Ahmadi, M.; Behafarid, F.; Gan, L.; Neumann, M.; Heggen, M.; Cuenya, B.R.; Strasser, P. Shape-selected bimetallic nanoparticle electrocatalysts: evolution of their atomic-scale structure, chemical composition, and electrochemical reactivity under various chemical environments. *Faraday Disc.* **2013**, DOI: 10.1039/C3FD20159G.
32. Cui, C.; Gan, L.; Heggen, M.; Rudi, S.; Strasser, P. Compositional segregation in shaped Pt alloy nanoparticles and their structural behavior during electrocatalysis. *Nature Mat.* **2013**, DOI: 10.1038/NMAT3668.
33. Cui, C.; Gan, L.; Li, H.-H.; Yu, S.-H.; Heggen, M.; Strasser, P. Octahedral PtNi Nanoparticle Catalysts: Exceptional Oxygen Reduction Activity by Tuning the Alloy Particle Surface Composition. *Nano Lett.* **2012**, *12*, 5885–5889.
34. Hasche, F.; Oezaslan, M.; Strasser, P. Activity, Structure and Degradation of Dealloyed $PtNi_3$ Nanoparticle Electrocatalyst for the Oxygen Reduction Reaction in PEMFC. *J. Electrochem. Soc.* **2012**, *159*, B25–B34.
35. Oezaslan, M.; Hasché, F.; Strasser, P. *In Situ* Observation of Bimetallic Alloy Nanoparticle Formation and Growth Using High-Temperature XRD. *Chem. Mater.* **2011**, *23*, 2159–2165.
36. Yu, C. F.; Holby, E. F.; Yang, R. Z.; Toney, M. F.; Morgan, D.; Strasser, P. Trajectories Growth and Coarsening Mechanisms of Metal Nanoparticle Electrocatalysts. *ChemCatChem* **2012**, *4*, 766–770.
37. Tuaev, X.; Strasser, P. Small Angle X-Ray Scattering (SAXS) Techniques for Polymer Electrolyte Membrane Fuel Cell Characterisation. In *Polymer Electrolyte Membrane and Direct Methanol Fuel Cell Technology*; Roth, C.; Hartnig, C., Eds.; Woodhead Publishing Series in Energy: London, 2011; Vol. II: In situ characterization techniques for low temperature fuel cells.
38. Oezaslan, M.; Heggen, M.; Strasser, P. Size-Dependent Morphology of Dealloyed Bimetallic Catalysts: Linking the Nano to the Macro Scale. *J. Am. Chem. Soc.* **2012**, *134*, 514–524.
39. Haas, S.; Zehl, G.; Dorbandt, I.; Manke, I.; Bogdanoff, P.; Fiechter, S.; Hoell, A. Direct Accessing the Nanostructure of Carbon Supported Ru-Se Based Catalysts by ASAXS. *J. Phys. Chem. C* **2010**, *114*, 22375–22384.
40. Petkov, V. Nanostructure by High-Energy X-Ray Diffraction. *Mater. Today* **2008**, *11*, 28–38.
41. Petkov, V.; Ohta, T.; Hou, Y.; Ren, Y. Atomic-Scale Structure of Nanocrystals by High-Energy X-Ray Diffraction and Atomic Pair Distribution Function Analysis: Study of Fe_xPd_{100-x} (x = 0, 26, 28, 48) Nanoparticles. *J. Phys. Chem. C* **2007**, *111*, 714–720.
42. Wang, C.; Markovic, N. M.; Stamenkovic, V. R. Advanced Platinum Alloy Electrocatalysts for the Oxygen Reduction Reaction. *ACS Catal.* **2012**, *2*, 891–898.
43. Stuhrmann, H. B. Resonance Scattering in Macromolecular Structure Research. *Adv. Polym. Sci.* **1985**, *67*, 123–163.
44. Stuhrmann, H. B.; Goerigk, G.; Munk, B. Anomalous X-Ray Scattering. In *Handbook of Synchrotron Radiation*; Ebashi, S.; Koch, M.; Rubinstein, E., Eds.; Elsevier: Amsterdam, 1991; Vol. 4, p 557.
45. Haubold, H.-G.; Wang, X. H.; Goerigk, G.; Schilling, W. *In Situ* Anomalous Small Angle X-Ray Scattering Investigation of Carbon Supported Electrocatalysts. *J. Appl. Crystallogr.* **1997**, *30*, 653–658.
46. Damaschun, G.; Muller, J. J.; Purschel, H. V.; Sommer, G. Computation of Shape of Colloidal Particles from Low-Angle X-Ray Scattering. *Mon. Chem.* **1969**, *100*, 1701–1714.
47. Walter, G.; Kranold, R.; Gerber, T.; Baldrian, J.; Steinhart, M. Particle Size Distribution from Small-Angle X-Ray Scattering Data. *J. Appl. Crystallogr.* **1985**, *18*, 205–213.
48. Scherrer, P. Bestimmung der Grösse und der Inneren Struktur Von Kolloidteilchen Mittels Röntgenstrahlen. *Nachr. Ges. Wiss. Göttingen* **1918**, *2*, 98–100.
49. Paredis, K.; Ono, L. K.; Mostafa, S.; Li, L.; Zhang, Z. F.; Yang, J. C.; Barrio, L.; Frenkel, A. I.; Cuenya, B. R. Structure, Chemical Composition, and Reactivity Correlations during the *in Situ* Oxidation of 2-Propanol. *J. Am. Chem. Soc.* **2011**, *133*, 6728–6735.
50. Yu, C. F.; Koh, S.; Leisch, J. E.; Toney, M. F.; Strasser, P. Size and Composition Distribution Dynamics of Alloy Nanoparticle Electrocatalysts Probed by Anomalous Small Angle X-Ray Scattering (ASAXS). *Faraday Discuss.* **2008**, *140*, 283–296.
51. Snyder, J.; Fujita, T.; Chen, M. W.; Erlebacher, J. Oxygen Reduction in Nanoporous Metal–Ionic Liquid Composite Electrocatalysts. *Nat. Mater.* **2010**, *9*, 904–907.
52. Mavrikakis, M.; Hammer, B.; Norskov, J. K. Effect of Strain on the Reactivity of Metal Surfaces. *Phys. Rev. Lett.* **1998**, *81*, 2819–2822.
53. Stamenkovic, V.; Mun, B. S.; Mayrhofer, K. J. J.; Ross, P. N.; Markovic, N. M.; Rossmeisl, J.; Greeley, J.; Nørskov, J. K. Changing the Activity of Electrocatalysts for Oxygen Reduction by Tuning the Surface Electronic Structure. *Angew. Chem., Int. Ed.* **2006**, *45*, 2897–2901.
54. Goerigk, G.; Haubold, H.-G.; Schilling, W. Kinetics of Decomposition in Copper-Cobalt: A Time-Resolved ASAXS Study. *J. Appl. Crystallogr.* **1997**, *30*, 1041–1047.
55. Kohlbrecher, J.; Bressler, I. *Software Package Sasfit for Fitting Small-Angle Scattering Curves*, 0.93.2; http://kur.web.psi.ch/sans1/SANSSoft/sasfit.html, 2010.
56. Tuaev, X.; Paraknowitsch, J. P.; Illgen, R.; Thomas, A.; Strasser, P. Nitrogen-Doped Coatings on Carbon Nanotubes and Their Stabilizing Effect on Pt Nanoparticles. *Phys. Chem. Chem. Phys.* **2012**, *14*, 6437–6440.
57. Proffen, T.; Petkov, V.; Billinge, S. J. L.; Vogt, T. Chemical Short Range Order Obtained from the Atomic Pair Distribution Function. *Z. Kristallogr.* **2002**, *217*, 47–50.
58. Farrow, C. L.; Juhas, P.; Liu, J. W.; Bryndin, D.; Bozin, E. S.; Bloch, J.; Proffen, T.; Billinge, S. J. L. Pdffit2 and Pdfgui: Computer Programs for Studying Nanostructure in Crystals. *J. Phys.: Condens. Matter* **2007**, *19*.